Titan Radar Mapper observations from Cassini's T₃ fly-by

C. Elachi[1], S. Wall[1], M. Janssen[1], E. Stofan[2], R. Lopes[1], R. Kirk[3], R. Lorenz[4], J. Lunine[4,5], F. Paganelli[1], L. Soderblom[3], C. Wood[6], L. Wye[7], H. Zebker[7], Y. Anderson[1], S. Ostro[1], M. Allison[8], R. Boehmer[1], P. Callahan[1], P. Encrenaz[9], E. Flamini[10], G. Francescetti[11], Y. Gim[1], G. Hamilton[1], S. Hensley[1], W. Johnson[1], K. Kelleher[1], D. Muhleman[12], G. Picardi[13], F. Posa[14], L. Roth[1], R. Seu[13], S. Shaffer[1], B. Stiles[1], S. Vetrella[11] & R. West[1]

Cassini's Titan Radar Mapper imaged the surface of Saturn's moon Titan on its February 2005 fly-by (denoted T₃), collecting high-resolution synthetic-aperture radar and larger-scale radiometry and scatterometry data. These data provide the first definitive identification of impact craters on the surface of Titan, networks of fluvial channels and surficial dark streaks that may be longitudinal dunes. Here we describe this great diversity of landforms. We conclude that much of the surface thus far imaged by radar of the haze-shrouded Titan is very young, with persistent geologic activity.

The Cassini Titan Radar Mapper[1,2] is a four-mode, K_u-band (wavelength = 2.17 cm) instrument. The synthetic-aperture radar (SAR) mode produces image data with best resolution of 300 m per pixel; scatterometry, altimetry and radiometry modes produce lower-resolution data. Here we report on data acquired during the T₃ fly-by and compare these with the T_A data, acquired in October 2004 at higher latitudes in the same hemisphere[3].

The T₃ encounter, with a closest approach at 30° N latitude, 70° W longitude, and 1,579 km altitude at 6:58 Universal Time Coordinated (UTC) on 15 February 2005, was Cassini's third fly-by of Titan and the first after the Huygens probe descent. Radar observations started with an inbound altimetry track covering an arc of ~8°, followed immediately by a 40-min SAR swath, symmetric about closest approach (Fig. 1a; an uncontrolled, higher-resolution version is in the Supplementary Information). The SAR imaging data covered approximately 1.8×10^6 km², with a spacecraft-to-surface range up to 5,500 km and a spatial resolution of 300–1,500 m. At 20 min after closest approach, an outbound altimetry track began, after which scatterometry scans extended from about 35° S to 50° N and 0° to 15° W, overlapping and extending similar coverage from T_A. Low-resolution radiometry was obtained concurrently with all other data types.

Mapping units

In the T_A SAR swath, five surface units were mapped, based solely on brightness variations, general plan-form shape, and texture[3]. These are not classified as material stratigraphic units (such as rock or ice) because we do not fully understand the relative contributions to SAR brightness from surface roughness, surface topography, material composition, and/or volume scattering. The T₃ swath contains all five of these units (dark homogeneous, mottled, dark mottled, bright lobate, and bright lineated) and three additional units (bright mottled, bright homogeneous, and bright rough) (see Fig. 2). Mapping in the T₃ swath is complicated by long and narrow dark features, occurring on all mapped units—except dark mottled and bright lobate—that are likely to be surficial deposits obscuring the underlying units.

The dominant unit in T₃, covering almost half of the swath and characterized by irregular bright patches of variable size, is a bright mottled unit (Fig. 2a and b) not seen in the T_A swath. Small (<10 km) bright spots in this unit may be topographic features. The second most extensive is the mottled unit (Fig. 2c), occurring in the eastern half of the swath. It includes gradational boundaries, moderate to bright backscatter, and outcroppings of the dark mottled unit. The bright homogeneous unit (Fig. 2d) occurs in the centre of the T₃ swath and contains a large impact crater and numerous channel-like features that we interpret as fluvial in origin. The low-backscatter and relatively featureless dark homogeneous unit (Fig. 2e), the most extensive in the T_A swath, occurs in the eastern portion of the T₃ swath.
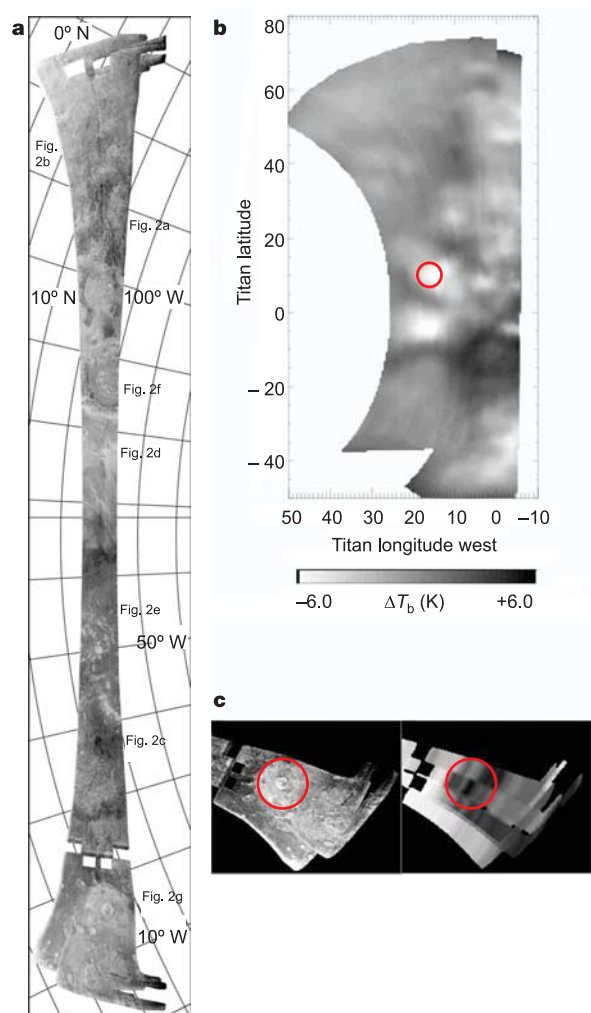
We identified a bright lobate unit in the T_A swath and interpreted it as cryovolcanic in origin on the basis of its resemblance in shape and brightness to SAR images of basaltic flows on Earth[3]. Fluvial or mass-wasting mechanisms are less likely possibilities, but the previous identification of two dome-like features[3,4] and theoretical considerations[4,5] also indicate that cryovolcanism probably happened on Titan. Three small features in the T₃ swath are mapped as the same bright lobate unit (Fig. 2e), though the relatively low spatial resolution in relation to the size of the features hinders interpretation. In T₃ these patches of bright lobate unit appear in association with two bright hills and a circular feature. The T_A bright lineated unit is an SAR-right, lineated unit with polygonal boundaries. It occurs in one location in the T₃ swath (Fig. 2d).

Our interpretation is that these were formed by a flowing material, in places confined by topography that may be tectonic in origin, because of its combination of fan-shaped and sinuous features. If this unit is a flow deposit it is probably composed of rough ice materials. The lineations are either produced by flow or are dark streaks

overlying the brighter underlying deposit. The bright lineated unit was also mapped in the T_A swath, both in association with fan-shaped and sinuous features and as an angular unit associated with dark terrain. The dark mottled unit, occurring in crescent-shaped patches in the T_A swath, was interpreted as smooth deposits, perhaps ponds of hydrocarbons[3]. Similar terrain, forming irregularly shaped patches tens of kilometres across, occurs in the eastern end of T_3 (Fig. 2c). No surficial streaks are seen on or associated with these patches, suggesting that the T_3 dark mottled unit may be liquids or smooth patches of particulates (ice sand) undisturbed by wind.

In the eastern part of the T_3 swath we have identified a bright rough unit (Fig. 2e), which consists of groups of materials that appear to be topographically high and rugged, as they exhibit evidence of both layover and topographic shading. These features are more distinct and noteworthy than the small hills found in the T_A unit. We interpret this material to be high-standing, fractured ice, older than the surrounding plains material that appears to embay it.

Impact craters

No impact craters were positively identified in the T_A SAR image swath[3]. The T_3 SAR swath is dominated by a 450-km-wide circular structure that is clearly an impact basin. A second, 80-km-diameter impact crater appears at the eastern end of T_3 and has been subsequently observed at infrared wavelengths[4,6]. Both craters occur in the bright homogeneous unit and on the boundary of the mottled and bright mottled units.

The 450-km-diameter double-ring impact basin, Menrva, is centred near 87° W, 19° N (Fig. 2f); its general shape is also seen in the near-infrared image shown as background[6]. The steep inner wall is bright, exhibiting radial lineaments, presumably grooves and chutes. The southern and western regions of the floor are relatively bland, suggesting resurfacing. The centre of the basin appears elevated and rough-textured, with a bright inner ring about 100 km in diameter. Dark, thin, linear streaks extend from the basin's lower wall onto the basin floor. The western rim shows more signs of erosion than the eastern rim. Candidate fluvial features, discussed below, may be associated with the basin.

The 80-km crater Sinlap, at 16° W, 11° N, shows no evidence of a raised rim (Fig. 2g). Craters of this diameter on Ganymede[7] have domed floors, probably due to viscous relaxation, and central pits. There is no indication of such features in Sinlap, nor of a central peak or peak ring. A 2- to 3-km bright spot appears 8 km west-southwest of the centre. The floor seems flat, similar to lava-flooded craters on the Moon or to craters with smooth deposits on Mars. Assuming that the crater wall has the same height and slope around its perimeter, we calculate[8] a wall slope of $16 \pm 5°$ and a crater depth of $1,300 \pm 200$ m for a depth/diameter ratio of 0.016 ± 0.03. The crater is asymmetrically surrounded by a blanket of SAR-bright material, presumably impact ejecta, biased towards the eastern side. In places it extends more than two crater radii beyond the rim, possibly arguing for some degree of fluidization of the ejecta[9]. No extensive distal ejecta deposits, such as rays or the typically SAR-dark parabolae seen on Venus, are observed.

This is a very small number of craters, far fewer than on airless, geologically inactive bodies. Titan's dense atmosphere should break up or slow small, incoming projectiles that would form craters of up to 20 m in diameter[10]. The presence of only one 450-km impact basin so far is not surprising; the distribution of such large craters on Rhea and Iapetus might imply several more comparably sized basins on Titan, though at this end of the size spectrum we expect very few[11]. It is surprising, however, that we have not detected significant numbers of craters with diameters between 20 and 100 km. If Titan's cratering rate is similar to Rhea's, more than 200 craters larger than 20 km in diameter should have formed in the ~2% of the surface sampled using SAR. Their absence suggests that they have been erased or buried by tectonic and/or cryovolcanic processes. If Titan's crust is or was very thin, it is also possible that viscous relaxation made most such craters extremely shallow, and these were subsequently buried, perhaps by organic aerosols sedimenting from the stratosphere. All these possibilities require additional radar observations to cover more of the surface (and possibly find partially buried structures).

Fluvial features

A variety of apparent drainage patterns are observable in the T_3 swath, some lighter and some darker than their surround. They include linear channel-like features (hereafter "channels") 1–2 km wide and tens to hundreds of kilometers long, and SAR-bright formations, apparently dendritic drainages (hereafter "drainages"), at various scales close to Menrva. In contrast to the external channels, which are all SAR-bright, the short channels on the inner rim of the basin are both darker and brighter in SAR than the surrounding material. A well-developed 2- to 4-km-wide example of the latter appears to flow generally eastward and terminates at the southwestern rim. Others, less branched, seem to flow generally northeast

Figure 1 | T_3 SAR swath. a, Full swath, indicating locations of enlargements shown in Fig. 2b. **b,** Relative brightness temperature ΔT_b accompanying the scatterometry in Fig. 3 for T_A outbound and T_3 passes. The red circle indicates a radiometrically cool feature surrounding the 80-km crater Sinlap, a feature shown at higher resolution in **c. c,** The left panel shows the end of the SAR strip with Sinlap and surrounding terrain, interpreted as an ejecta blanket. The right panel shows the accompanying radiometry. The red circle defines the same area as in **b.** Spatial resolution is determined by the footprints of the five SAR beams spanning the strip.

from just outside the southeast rim of the crater for about 200 km and terminate in a series of fan-shaped, delta-like forms that coalesce into a bright region, possibly a collecting basin. These channels include meandering, linear, and braided segments, with widths ranging from the limit of SAR resolution to 7 km. The arrangement of all these features suggests an E-to-NE downward regional slope. Several very different drainages appear along the inner rim of the crater, most prominently on the eastern side. These systems are short, 20–50 km long, tightly branched, with branches 1–2 km wide, extending roughly radially into the crater.

SAR backscatter of the large drainage patterns outside Menrva at various incidence angles is consistently 2 to 3 dB greater than that of the surrounding terrain. The SAR-bright area formed by coalescing channels east of the crater is large enough to be resolved by the Cassini imaging system and also appears bright at 0.93 µm (ref. 6). The dark/bright modulation of the shorter channels strongly suggests resolved topographic slopes. Radarclinometric modelling and a consideration of the geometric distortion of these features indicate that they are 200–300 m deep, with inward-facing slopes of the order of 10°; uncertainty in the assumed backscatter curve and the limited resolution of the images lead to errors of at most 50% in these depth estimates.

We suggest that the SAR-observed channels are produced by low-viscosity fluids, possibly liquid methane, as appears to be the case for smaller channels observed in the Huygens descent images[12]. However, we cannot rule out participation of ammonia-water cryo-lava in the creation of the larger channels at temperatures enough above the eutectic to keep viscosity relatively low[13]. We regard ammonia-water fluid as a less likely agent than liquid hydrocarbons because we do not see evidence that the T_3 channels terminate in formations like those interpreted as flow lobes in the T_A data[3]. In the T_A channels, heating associated with volcanism might have created fractures along which liquid hydrocarbons flowed and carved channels, while in the T_3 region the causative agent of crustal fracturing was the large impact. Whether these processes also acted to liberate liquid hydrocarbons stored in the crust, or whether liquid was supplied by precipitation, cannot be determined from the data at hand.

Surficial dark streaks

Dark lineated streaks occur in regions of variable extent throughout the T_3 swath (Fig. 2a, f and g). The area of such regions ranges from 500 km^2 near the southeastern rim of the large basin to 35,000 km^2 in the western part of the swath, in total occupying approximately 10% of the T_3 swath. They appear in places to have an abrupt termination, possibly controlled by change of topography (for example, west of the basin), while in other places they blend and disappear in the surrounding surfaces (for example, the centre of the swath and west of the basin) or divert and wrap around the bright material of Sinlap. Individual streaks are ≤50 km in length, 500 m to 1 km across, and separated by 1–2 km. They are straight or sinuous, with prevalent orientation within 30° of east–west. Streak spacing for an informal sampling is 1.5 ± 0.4 km. The SAR expression of these features is typically as uniform dark bands, except in a few cases where there is some suggestion of a flanking bright edge.

The morphological characteristics and relationships of the dark streaks with the surrounding surfaces and orientation of Y-shaped junctions suggest they could represent linear (longitudinal) dunes formed by eastward aeolian (wind-generated) transport and accumulation, although they could as well be wind streaks with little or no topography. Longitudinal dunes imply a variable but typically bidirectional wind regime that is on average parallel to the dunes' long direction. SAR images of terrestrial dunes show similar patterns[14]. Remarkably similar images of snow dunes in Antarctica show alternating light and dark bands with narrow, low-backscatter bands alternating to wider, high-backscatter ones, which imply variation in grain size; these are also reported to have little topographic expression[15]. Radiometry observations of the Titan streaks are medium-bright, consistent with low-volume scattering, therefore suggesting a shallow-depth, grain-scale scattering effect.

Sources of sediments or particulate materials feeding aeolian dunes on Titan could include water ice, water-ammonia ice, solid hydrocarbons and nitriles such as acetylene, hydrogen cyanide, and other organic solid clathrates. It has been hypothesized[16] that sand-sized material might be produced from a mix of such materials as
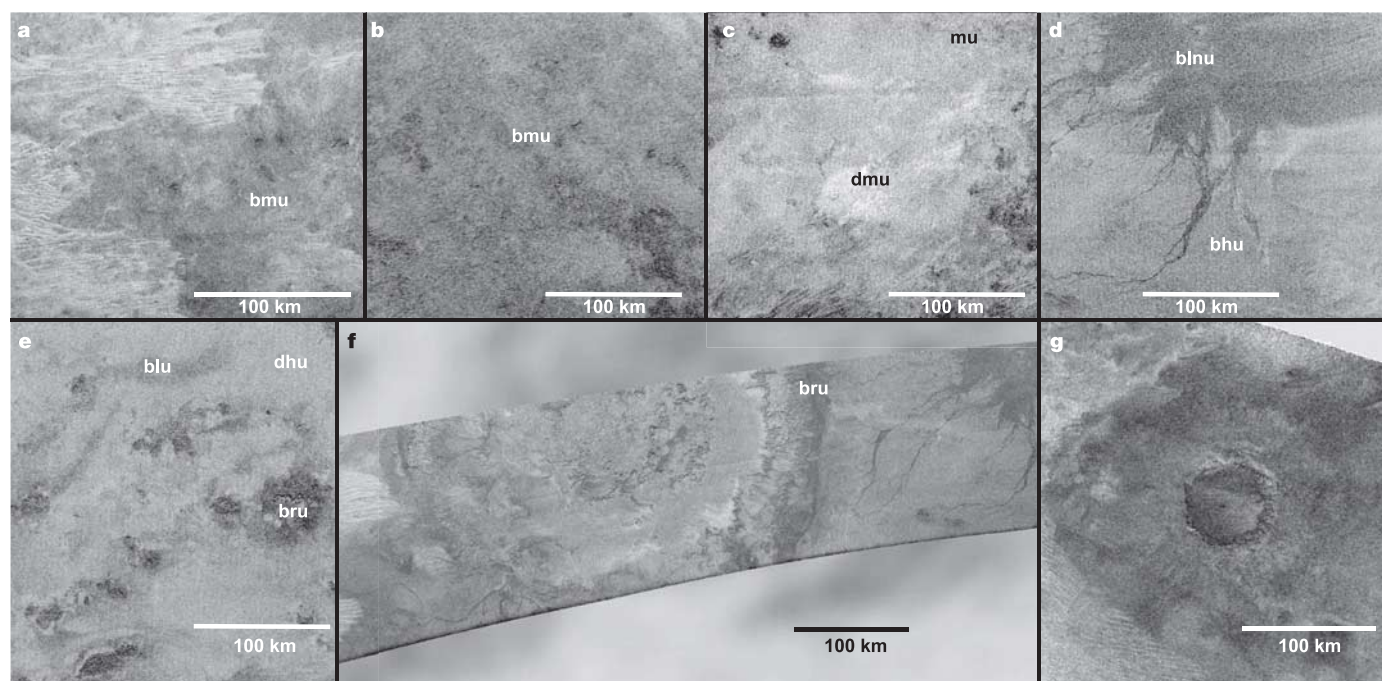
Figure 2 | Discrete mapping units in the T_3 SAR swath. Included are three units not detected in T_A: bmu (bright mottled unit), bhu (bright homogeneous unit) and bru (bright rough unit) (segments individually enhanced). **a** and **b**, bmu. **c**, mu (mottled unit); dmu (dark mottled unit). **d**, bhu; blnu (bright lineated unit). **e**, bru; blu (bright lobate unit); dhu (dark homogeneous unit). **f**, 450-km impact basin Menrva (note ISS image in background). **g**, 80-km crater Sinlap.

impact ejecta; Huygens probe observations of channel networks suggest that fluvial erosion could also represent a viable source of sediments. Probe data indicate winds of ~0.3 m s^{-1} in the lowest part of its descent[12]; such wind speeds are comparable with the threshold speeds needed to transport (saltate) sand-sized particles in Titan's low gravity and thick atmosphere[16]. Winds of this magnitude have been predicted to be generated by Saturn's gravitational tide on Titan[17] or by Titan's super-rotation, the resultant wind being almost entirely prograde (eastward). Cassini Imaging Subsystem (ISS) data have shown evidence of predominantly east–west aeolian features that suggest an eastward wind direction[6].

Although dune patterns appear over a large portion of the T$_3$ swath, they do not appear in areas dissected by bright channels. The mobile dark material could also form the more amorphous dark patches observed in the radar data (for example, the dark mottled unit in Fig. 2).

### Physical and electrical surface properties

To the SAR data, scatterometry and radiometry add information on the physical and electrical properties of the surface. T$_3$ scatterometry also observed the same terrain seen at the end of the T$_3$ SAR strip, yielding higher-resolution backscatter measurements. Relatively high-resolution radiometry data were obtained in both SAR and scatterometer passes between the active radar echoes.

A comparison of the common area covered by the scatterometer in T$_A$ outbound and T$_3$ passes is presented in Fig. 3. Although there are several notable differences, the main one is that Sinlap is seen in the T$_A$ outbound scan. Various specular scattering models have been successfully applied to planetary surfaces; although statistically acceptable fits result (see Fig. 3), the uncertainty in least-squares parameter estimates is large. We are not satisfied that the modelling of the current data establishes meaningful bounds on key physical quantities (for example, dielectric constant and root-mean-square slope). Nonetheless, it is clear that we are seeing a smooth surface component with low-to-moderate effective dielectric constants. We note that the scattering functions pictured in our plots are built up from measurements of diverse locations, in contrast with the

more-usual scatterometric observation of a specific location at multiple angles. Thus, in modelling, we are implicitly trying to average over potentially very diverse locations. Moreover, the nature of radar scattering from Titan may be intrinsically different from that encountered on other planetary radar targets.

Figure 1b shows the radiometric measurements obtained during the T$_3$ scatterometry pass and the T$_A$ outbound pass. Regions of low radiometric brightness are strongly correlated with regions of high radar reflectivity in Fig. 3. Because the physical temperature variations are likely to be relatively small over this limited area, brightness variations can be ascribed to variations in emissivity rather than temperature. These in turn reflect variations in the physical or chemical properties of the surface. The observed radiometric temperature could result either from variations in the dielectric constant of near-surface material, or from variations in the degree of subsurface (volume) scattering. In the case of surface scattering, a high dielectric constant generally leads to high reflectivity and consequently low emissivity and brightness temperature. On the other hand, a lower surface dielectric constant can result in a decrease in brightness temperature if there is enhanced scattering from the subsurface. The correlation of radar reflection and low emissivity is most simply explained by the presence of enhanced volume scattering in the radar-reflective, radiometrically cool regions. However, this explanation is not unique, because the radiometrically dark regions could also have a higher dielectric constant to account for the lower emissivity and higher roughness to account for the radar return.

A feature associated with Sinlap is seen in both radiometry and scatterometry data and coincides approximately (within the radiometer/scatterometer resolution) with the bright halo. Figure 1c compares the eastern end of the T$_3$ SAR strip (left) with the accompanying radiometry (right). As discussed above, the decrease in emissivity of the ejecta could be explained by an increase in dielectric constant and the lack of volume scatter, suggesting, for example, an increase in dielectric constant from 2 to 3. Alternatively, the decrease in emissivity as well as the increased scattering seen both in the SAR swath and in the scatterometry could be due to increased
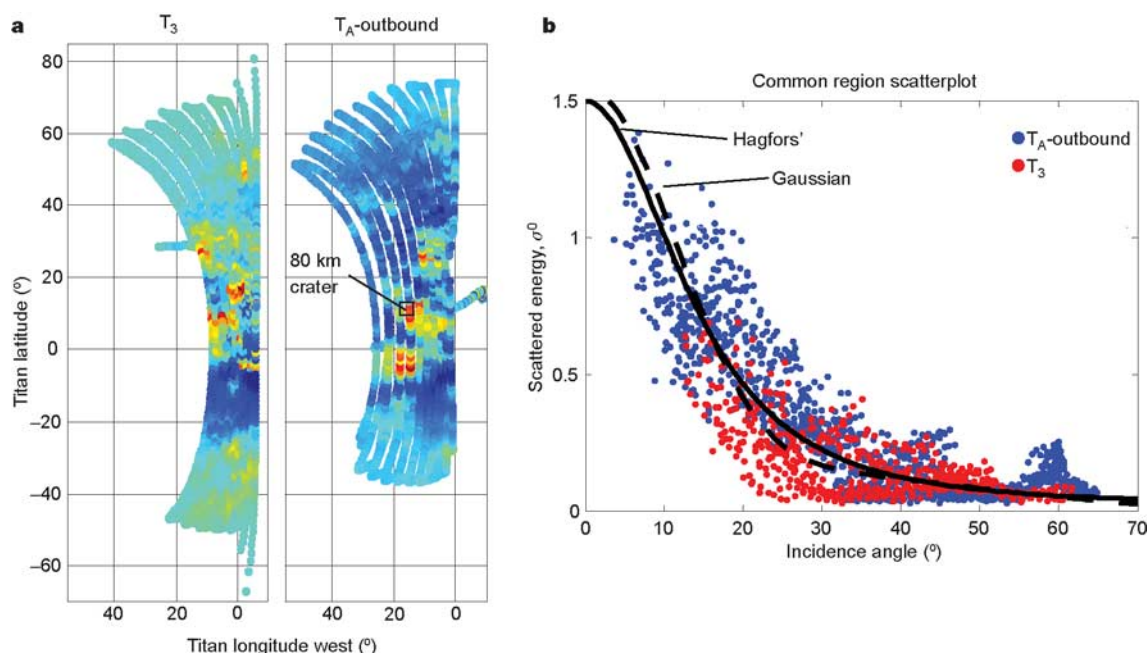
Figure 3 | Comparison of T$_A$ outbound and T$_3$ scatterometry, showing consistency of measurements. a, The 80-km crater Sinlap is indicated. The plot of relative scattered energy σ^0 versus incidence angle from the common region in **b** is equally well fitted by several models. Pictured here are a

Hagfors specular scattering model, and a combination of a gaussian model and a cosine-like volume-scattering term. The Hagfors curve suggests a surface with a high dielectric constant (5), while the gaussian model implies a much lower value (<2).

volume scattering alone. More detailed modelling is needed to examine whether a similar dielectric constant change could explain the observed increase in SAR brightness as well, or whether volume scattering increases are required.

Discussion

The T_A and T_3 swaths cover approximately 3% of the surface of Titan. Two impact craters appear in the T_3 swath, whereas no unambiguous impact craters could be identified in the T_A swath. From the scarcity of 20–100 km craters observed, we conclude that the surface of Titan is predominantly young. The ubiquitous dark streaks in the T_3 swath we interpret as resulting from aeolian processes. Their presence indicates a relatively large amount of material capable of being transported and redeposited. This mobile material may be produced by fluvial or aeolian erosion or atmospheric deposition. As in the T_A swath, we see no clearly identifiable large bodies of liquid.

Both swaths provide ample evidence that Titan has been resurfaced recently in its geologic history. Both impact craters in the T_3 swath have been modified by erosion and infilling. The bright rough unit also provides support for modification and burial of older surfaces. Probable resurfacing processes include cryovolcanism, fluid flow, aeolian processes, and atmospheric deposition. In contrast to T_A, the T_3 swath contains no convincing examples of bright lobate flow features indicative of cryovolcanism. There are no structures similar to Ganesa Macula found in the T_A swath[3]. The T_3 swath is farther south than T_A, but at present there is insufficient coverage to determine whether cryovolcanic features are widespread and randomly distributed, or exhibit some geographic pattern.

Evidence for fluid flow appears in both swaths in sinuous, channel-like features, or fan-shaped deposits. A fluvial origin for these features has been bolstered by the identification of apparent drainage channels in the Huygens image data[12], although channels in the latter are at a much smaller scale than those in the T_A and T_3 swaths. We interpret the degradation of the southwest part of the impact basin rim as being caused by fluid flow.

Radar data of both T_A and T_3 swaths suggest that volume scattering may be occurring. Therefore, some of the features and textures in the swaths may be produced by subsurface changes in composition or roughness. The striking difference in overall appearance of the two swaths—with T_A seemingly dominated by endogenic processes, and T_3 more reflective of atmospheric and impact-related effects—emphasizes the diverse nature of Titan's surface and provides justification for the expectation of entirely new surface landforms yet to be detected in additional SAR images and other radar data.

1. Elachi, C. *et al.* Cassini Titan Radar Mapper. *Proc. IEEE* **79**, 867–880 (1991).
2. Elachi, C. *et al.* RADAR: The Cassini Titan Radar Mapper. *Space Sci. Rev.* **117**, 71–110 (2005).
3. Elachi, C. *et al.* Cassini radar views the surface of Titan. *Science* **308**, 970–974 (2005).
4. Sotin, C. *et al.* Release of volatiles from a possible cryovolcano from near-infrared imaging of Titan. *Nature* **435**, 786–789 (2005).
5. Mitri, G., Lunine, J., Showman, A. & Lopes, R. Resurfacing of Titan by ammonia-water cryomagma. *Icarus* (submitted).
6. Porco, C. *et al.* Imaging of Titan from the Cassini spacecraft. *Nature* **434**, 159–168 (2005).
7. Schenk, P. Central pit and dome craters: Exposing the interiors of Ganymede and Callisto. *J. Geophys. Res.* **98**, 7475–7498 (1993).
8. Kirk, R. *et al.* & the Cassini Radar Team. RADAR reveals Titan topography. *Proc. 36th Annu. Lunar Planet. Sci. XXXVI* abstr. 2227 (2005).
9. Melosh, H. *Impact Cratering: A Geologic Process* 87–111 (Oxford Univ., Oxford, 1989).
10. Lorenz, R. Impacts and cratering on Titan: A pre-Cassini view. *Planet. Space Sci.* **45**, 1009–1019 (1997).
11. Wood, C., Lopes, R., Stofan, E., Paganelli, F. & Elachi, C. Impact craters on Titan? Cassini RADAR view. *Proc. 36th Annu. Lunar Planet. Sci. XXXVI* abstr. 1117 (2005).
12. Tomasko, M. G. *et al.* Rain, winds and haze during the Huygens probe's descent to Titan's surface. *Nature* **438**, 765–778 (2005).
13. Kargel, J., Croft, S., Lunine, J. & Lewis, J. Rheological properties of ammonia-water liquids and crystal-liquid slurries: Planetological applications. *Icarus* **89**, 93–112 (1991).
14. Blom, R. & Elachi, C. Spaceborne and airborne imaging radar observations of sand dunes. *J. Geophys. Res.* **86** (B4), 3061–3073 (1981).
15. Fahnestock, M., Scambos, T., Shuman, C., Arthern, R., Winebrenner, D. & Kwok, R. Snow megadunes fields on the East Antarctica Plateau: Extreme atmosphere-ice interaction. *Geophys. Res. Lett.* **27**(22), 3719–3722 (2000).
16. Lorenz, R., Lunine, J., Grier, J. & Fisher, M. Prediction of aeolian features on planets: Application to Titan paleoclimatology. *J. Geophys. Res.* **100**, 26377–26386 (1995).
17. Tokano, T. & Neubauer, F. Tidal winds on Titan caused by Saturn. *Icarus* **158**, 499–515 (2002).

Author Contributions C.E. is the RADAR Team Leader. All authors contributed equally to this work.

Author Information Reprints and permissions information is available at npg.nature.com/reprintsandpermissions. The authors declare no competing financial interests. Correspondence and requests for materials should be addressed to S.W. (steve.wall@jpl.nasa.gov).

CORRIGENDUM

Titan Radar Mapper observations from Cassini's T₃ fly-by

C. Elachi, S. Wall, M. Janssen, E. Stofan, R. Lopes, R. Kirk, R. Lorenz, J. Lunine, F. Paganelli, L. Soderblom, C. Wood, L. Wye, H. Zebker, Y. Anderson, S. Ostro, M. Allison, R. Boehmer, P. Callahan, P. Encrenaz, E. Flamini, G. Francescetti, Y. Gim, G. Hamilton, S. Hensley, W. Johnson, K. Kelleher, D. Muhleman, G. Picardi, F. Posa, L. Roth, R. Seu, S. Shaffer, B. Stiles, S. Vetrella & R. West

In this Article, Fig. 2 was printed in reverse (bright areas appeared dark and vice versa). The correct figure is reprinted below.